SUPPORTING INFORMATION

Evidence for Anisotropic Electronic Coupling of Charge Transfer States in Weakly Interacting Organic Semiconductor Mixtures

Valentina Belova*[,1], Paul Beyer[2], Eduard Meister[3], Theresa Linderl[3], Marc-Uwe Halbich[4], Marina Gerhard[4], Stefan Schmidt[3], Thomas Zechel[3], Tino Meisel[2], Alexander V. Generalov[5], Ana Sofia Anselmo[6], Reinhard Scholz[7], Oleg Konovalov[8], Alexander Gerlach[1], Martin Koch[4], Alexander Hinderhofer[1], Andreas Opitz*[,2], Wolfgang Brütting*[,3], Frank Schreiber*[,1]

1 – Institut für Angewandte Physik, Universität Tübingen, Tübingen 72076, Germany
2 – Department of Physics, Humboldt-Universität zu Berlin, Berlin 10099, Germany
3 – Institute of Physics, Experimental Physics IV, University of Augsburg, Augsburg 86135, Germany
4 – Faculty of Physics and Material Sciences Center, Philipps-Universität Marburg, Marburg 35037, Germany
5 – Max IV Laboratory, Lund University, Lund SE-221 00, Sweden
6 – Helmholtz-Zentrum Berlin für Materialien und Energie GmbH, Berlin 14109, Germany
7 – Dresden Integrated Center for Applied Physics and Photonic Materials (IAPP),
Technische Universität Dresden, Dresden 01187, Germany
8 – European Synchrotron Radiation Facility, Grenoble 38000, France

Table of Contents

AFM

AFM images (1×1 μm) of the studied samples are shown in Figure S1 with corresponding surface profiles. Clear molecular terraces are visible only for DIP. All mixtures reveal very smooth surfaces, although 1:1 is rougher than non-equimolar samples.

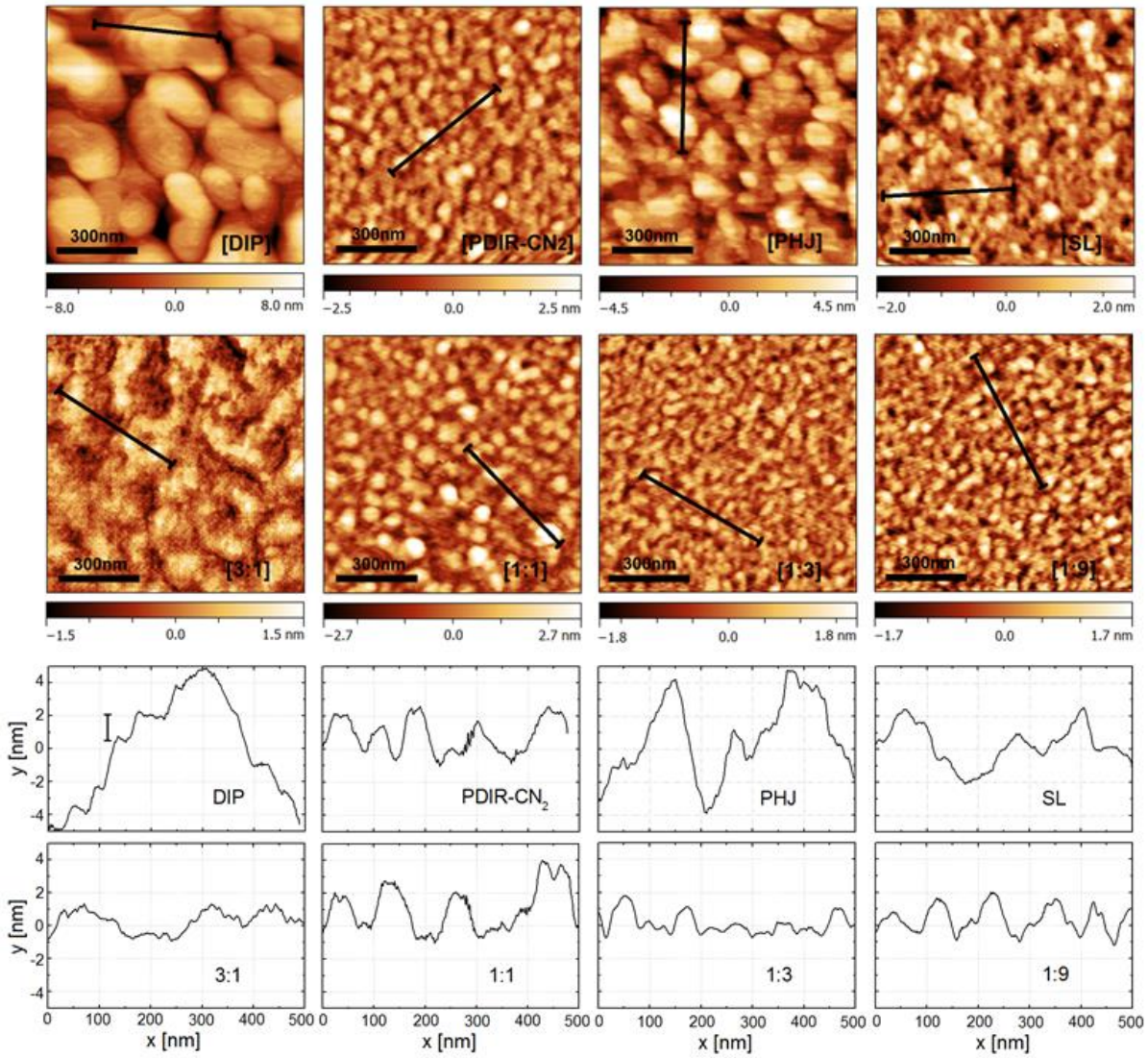

Figure S1 AFM images with surface profiles.

X-ray diffraction

Table S1 compiles film parameters extracted from fits of the Kiessig oscillations (XRR scans in Figure 4). The film roughnesses from AFM measurements are given for comparison. The lattice spacings are estimated from Bragg peak maximum positions defined by Gaussian fits.

Table S1 Summary of film parameters extracted from XRR fits and AFM roughnesses.

config.	thickness d (nm)	roughness σ (nm)	roughness AFM σ_{RMS} (nm)	$d_{(001)}$ (Å)
DIP	19.8	3.8	3.9	16.85
3:1	20.5	0.9	0.5	-
1:1	25.3	1.3	1.0	-
1:3	23.8	1.0	0.6	-
1:9	23.8	1.3	0.7	-
PDIR-CN_2	20.3	1.4	0.8	17.12
PHJ	42.9	3.2	1.8	16.85/17.12
SL	37.9	1.4	0.8	17.17

GIXD spectra of heterostructures (Figure S2) reveal only features of pristine materials.

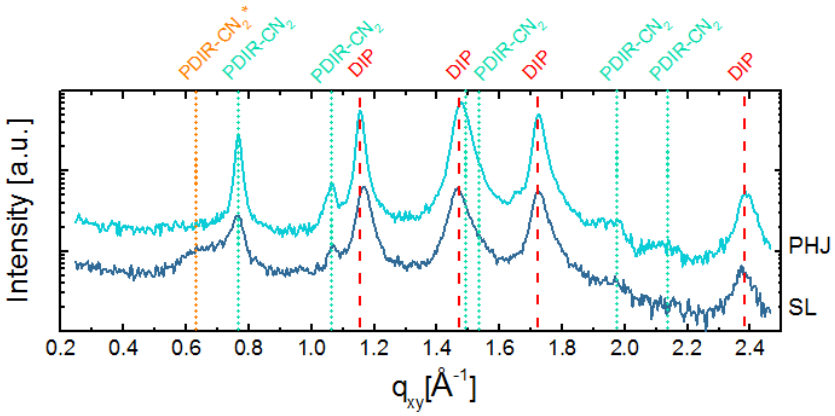

Figure S2 GIXD scans of PHJ and SL.

Ultraviolet photoelectron spectroscopy

We used ultraviolet photoelectron spectroscopy (UPS) to determine the HOMO level and the work function of the crystalline molecular films. Through this method, we also gain access to the ionization energies (IE) of the molecules in the layers. Valence band spectra for pristine DIP and PDIR-CN_2 thin films are shown in Figure S3. All energy values are derived from the peak onsets, calculated by linear extrapolation of the inflection point to the base line.

Due to the high degree of structural compatibility between DIP and the HOPG surface, the resulting templating effect forces the adsorbed molecules to grow in a mainly lying down fashion. On weakly interacting, amorphous surfaces, like SiO_2 or HIL 1.3 coated ITO, on the other hand, no such templating exists and the molecules grow rather upright standing. This large orientational difference conforms well to the lower IE (5.4 eV) for upright standing than for lying down (5.8 eV) DIP molecules.[1] According to our NEXAFS results (see the next part) PDIR-CN_2 does not experience strong interaction with the HOPG substrate since no significant orientational change was found (Figure S8). Nevertheless we can observe the IE shift by 0.3 eV from 7.1 eV on SiO_2 to 6.8 eV on HOPG (Figure S3c,d). LUMO level pinning is observed from the increase of work function upon deposition of PDIR-CN_2 on SiO_2 (see figure S3b).[2,3] By assuming a position of the pinned LUMO level of about -0.4 eV, the transport gap is 2.65 eV.[4,5]

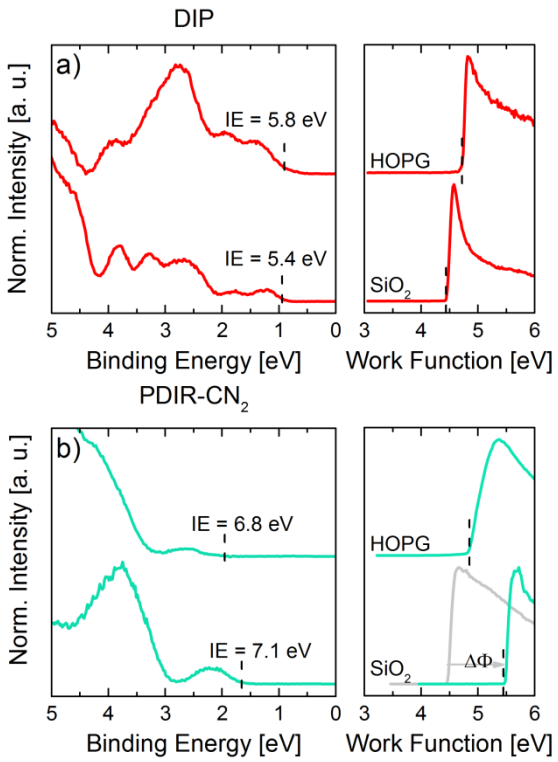

Figure S3 Valence region spectra and work functions of pristine (a) DIP and (b) PDIR-CN_2 thin films on amorphous SiO_2 (bottom) and highly oriented pyrolytic graphite (HOPG) substrates (top). The substrate contributions have been subtracted from the measured signal, in order to obtain the true molecular valence signatures. Dashed lines give the position of the HOMO and work function onsets, as determined by linear extrapolation of the inflection point to the baseline. The gray spectrum shows the work function of the uncovered SiO_2 substrate. $\Delta\Phi$ shows the work function shift and thus LUMO pinning of pristine PDIR-CN_2 films. All spectra are vertically scaled and shifted for clarity.

After the establishment of energy values of the pristine molecules, we now look at the energetic interplay at PHJ and PMHJ. We used ITO/HIL1.3 and HOPG substrates to build a base layer consisting of standing and lying DIP molecules, respectively. The results are shown in Figure S4.

Changing the substrate to HOPG results in a higher IE and vacuum level alignment of DIP to the substrate. The same is true for the deposition of PDIR-CN_2 on top, however, the IE changes only marginally (6.65 eV compared to 6.75 eV on standing DIP molecules), since the side groups of PDIR-CN_2 inhibit close stacking to the DIP molecules. To look at large-area D/A interfaces we evaporated blends of DIP and PDIR-CN_2 on top of DIP pre-covered ITO/HIL 1.3 and HOPG substrates. The results on the PMHJ on HOPG show the same trend as on ITO/HIL 1.3 and are shown in Figure S4d. In comparison to the energy levels of the pristine molecules, this strongly indicates a mixture containing upright-standing DIP molecules, breaking the templating effect of the HOPG substrate. We note further that a clear trend in IE of films dependent on molecular orientation as observed for other materials before[6-8] is absent for PDIR-CN_2.

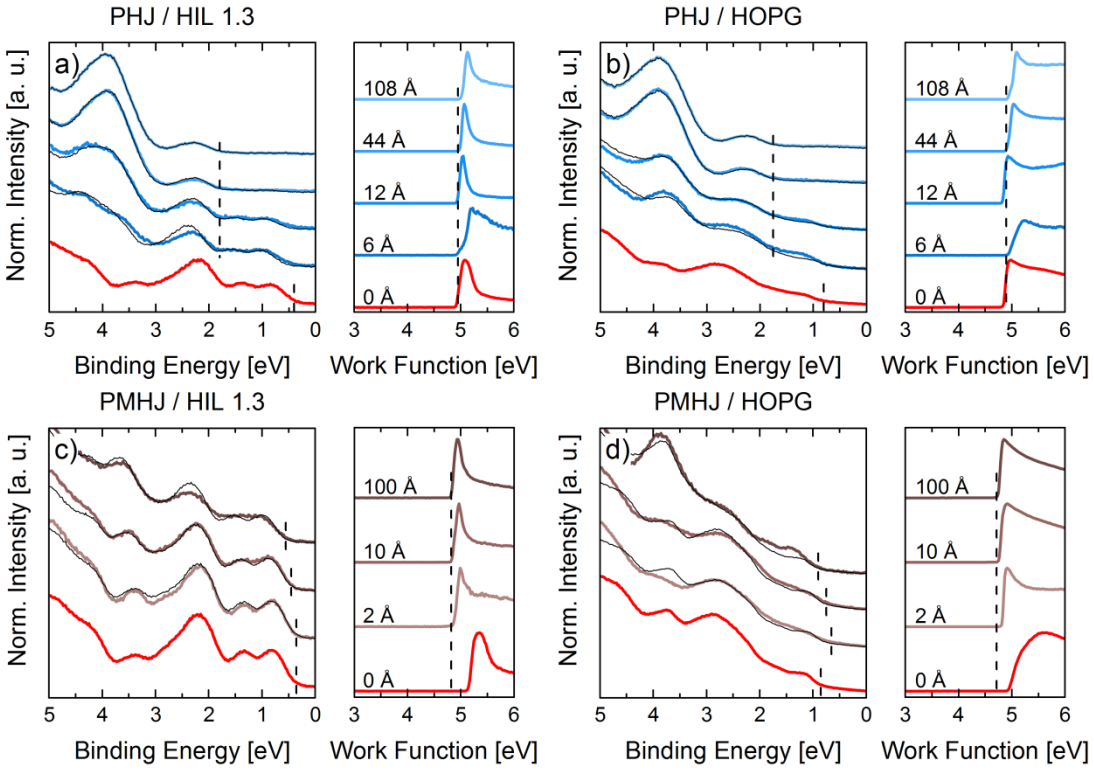

Figure S4 Valence region spectra and work functions (WF) of PHJ (a) on HIL 1.3 and (b) highly oriented pyrolytic graphite (HOPG) for increasing layer thicknesses, indicated by the inset values in the WF plots. The red graphs show the base line spectra of DIP covered substrates. Parts (c) and (d) show the analogous results of PMHJ architectures. All spectra are vertically scaled and shifted for clarity. Overlaid in the valence region spectra are fits with pristine valence signatures for all thicknesses in thin black curves.

NEXAFS

All samples for the NEXAFS measurements were deposited under high vacuum conditions (base pressure 10^{-7} mbar) and nominal growth rates of 4 nm/min for DIP and 3 nm/min for PDIR-CN_2. The NEXAFS measurements were performed at the beamline D1011 of the synchrotron storage ring MAX II at MAX IV laboratory, Lund University, Sweden. The used light is linearly polarized. Through the end station an energy resolution of about 50 meV around the carbon *K*-edge is achieved. All NEXAFS spectra were recorded in total electron yield mode. Contributions from the substrate, which overlap with the sample signature, were subtracted to isolate the unadulterated thin film spectra. The observed dichroisms were analysed using eq. (1), to obtain the average molecular orientation[9,10].

$$I_{\pi^*}(\theta,\alpha) \propto P \cdot \cos^2(\theta) \cdot \left(\frac{3}{2}\cos^2(\alpha) - \frac{1}{2}\right) + \frac{1}{2}\sin^2(\alpha) \qquad (1)$$

Here, Θ is the angle of incidence between the incoming X-ray photons and the sample surface plane, α is the average molecular inclination angle between molecular plane and substrate surface and P = 0.975 is the degree of polarization, characteristic for the beamline. Additionally, an angular offset Θ_{Offset} was introduced during the fit routine, to account for small angular misalignment of the sample. Since eq. (1) is symmetric around Θ = 90°, the last data point (Θ = 90° + Θ_{Offset}) was mirrored to (Θ = 90° - Θ_{Offset}) to achieve visual uniformness, without loss of generality.

Utilizing the dichroism of X-ray absorption, NEXAFS spectroscopy allows the determination of the average molecular orientation in thin films, perfectly supplementing the information gained from

XRD. The exact intensity dependence for π*-transitions for substrates of at least threefold-symmetry is given by eq. (1).[10]

To unambiguously identify the molecular arrangement at the interface, we complement our XRD measurements with NEXAFS spectroscopy at the C1s edge. The resulting absorption spectra are shown in Figure S5, Figure S6 and Figure S7. Pristine DIP on SiO_2, Figure S5a, shows clear dichroic behavior. After integration from 283.3 to 286.3 eV and angular analysis of the obtained π*-peak intensities using eq. (1), we obtain an average molecular inclination angle of 78±5° between molecular and substrate surface plane.[11] On HOPG, the reverse dichroism is clearly observed (Figure S6a). After subtraction of the C1s substrate signature,[12] analysis here yields an average molecular inclination angle of 33±5°. Since the carbon frame of the DIP molecules features a perfect lattice match to the HOPG surface, this dichroism is readily explained by the templating function of the HOPG to induce a new polymorph, consisting of lying down DIP molecules. Deviations from 0° for perfectly flat lying down molecules originate from defects on the substrate surface, as well as the averaging nature of the NEXAFS technique itself, being sensitive to both, crystalline (well-ordered) and amorphous (disordered) regions. This shows that the choice of HOPG and SiO_2 as substrates is ideal to control the molecular orientation of the DIP molecules, which is essential to control the orbital overlap at (organic-organic) interfaces.

Likewise, the X-ray absorption spectra of pristine PDIR-CN_2 on HOPG and SiO_2 are shown in Figure S5b and Figure S6b. In contrast to DIP, there is no clear dichroism visible, independent of the substrate choice. The results of the peak intensity evaluation are shown in Figure S8. On SiO_2 an average inclination angle of 55±5° is obtained, compared to 53±5° on HOPG. However, since we observe different IEs on both substrates, the molecular arrangements appear to be different. The templating function of the HOPG is reduced by the alkyl side chains of the PDIR-CN_2 molecules. On weakly interacting SiO_2, on the other hand, the undisturbed, known crystal phase with an average inclination angle of 53°[13] is adopted almost exclusively.

Looking at the X-ray absorption spectra of device relevant architectures in Figure S7a (PHJ) and b (PMHJ), we can identify features from both pristine components. Deconvoluting the mixed spectra with pristine spectra obtained at Θ=55° reproduces all major features. The best fits are shown by thin black lines in Figure S7. Angular analysis of the individual components isolates the separate orientations for DIP and PDIR-CN_2 molecules (Figure S9). The DIP molecules at the planar interface possess an average inclination angle of 79±5°, decreasing slightly at the mixed interface to 76±5°. For the PDIR-CN_2 contribution, the inverse trend is observed – a slight increase from 53±5° to 58±5°. This shows that the average orientation of both individual molecules in the planar configuration is nearly unperturbed compared to the pristine molecular films in the known crystal bulk structures. However, in the mixed film, where the interplay between donor and acceptor is much more pronounced, an angular shift towards a common alignment is achieved. This points towards a relaxation or segregation from the individual polymorphs to a new one, which was also seen in the GIXD data. The observed shift of at most 5° here is not astoundingly large. However, since NEXAFS determines only average orientations over all probed molecules, a much larger angular shift (>15°) due to relaxation in the new polymorph is most likely, while the individual pristine crystalline phases of DIP and PDIR-CN_2 coexist as well to some degree.

As mentioned before, no new features due to interaction are observed. This is shown in Figure S7 by the small residuals. There are several explanations for this distinction, for example forbidden dipole transitions, the weak interaction character of the ground state CT complex itself or just surface effects.[14-20] IR spectroscopy was performed in transmission mode, being sensitive to properties of the complete bulk. NEXAFS sensitivity, on the other hand, is limited by the inelastic mean free path of the excited electrons (~1nm) and the absorption depth of the incident X-ray photons, meaning that only surface properties are measured.[21] The weak interaction strength points towards a small overlap

in the ground state between both involved molecules, possibly too weak to be easily detected by the used setup. Additionally, the formed exciton upon optical or X-ray absorption involves different molecular orbitals. This results in the observed additional features for optical absorption, which are absent compared to X-ray absorption.

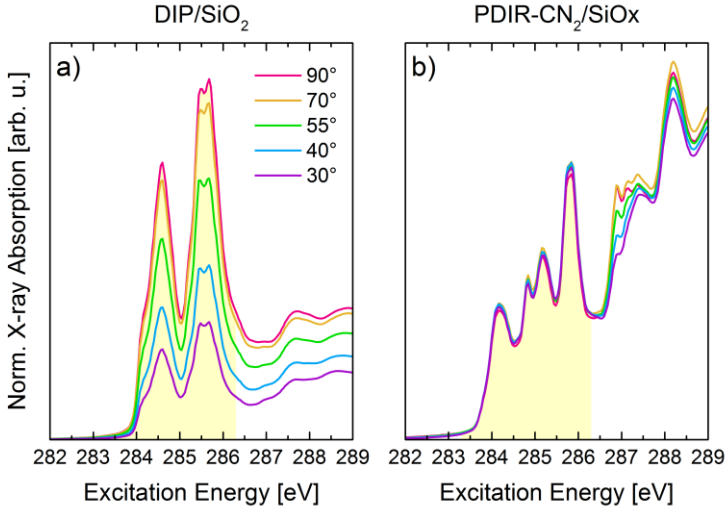

Figure S5 X-ray absorption spectra for varying angles of incidence Θ between the photon beam and the sample surface. The shaded area depicts the region used for obtaining the integrated peak intensities. Here, the results on amorphous SiO_2 substrates are shown for DIP (a) and PDIR-CN_2 (b). All spectra are normalized to the incident photon flux and to the C1s step edge at 270 and 330eV.

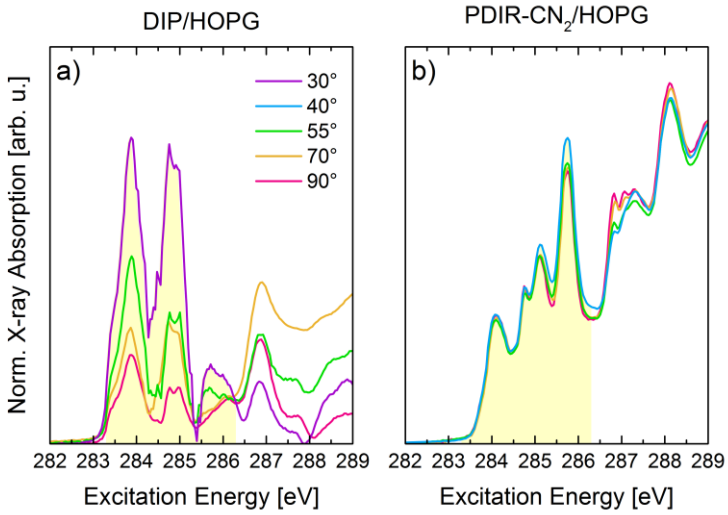

Figure S6 X-ray absorption spectra for varying angles of incidence Θ between the photon beam and the sample surface. The shaded area depicts the region used for obtaining the integrated peak intensities. Here, the results of DIP (a) and PDIR-CN_2 (b) on highly oriented graphite (HOPG) substrates are shown. Substrate contributions from the HOPG substrate were subtracted. All spectra are normalized to the incident photon flux and to the C1s step edge at 270 and 330eV.

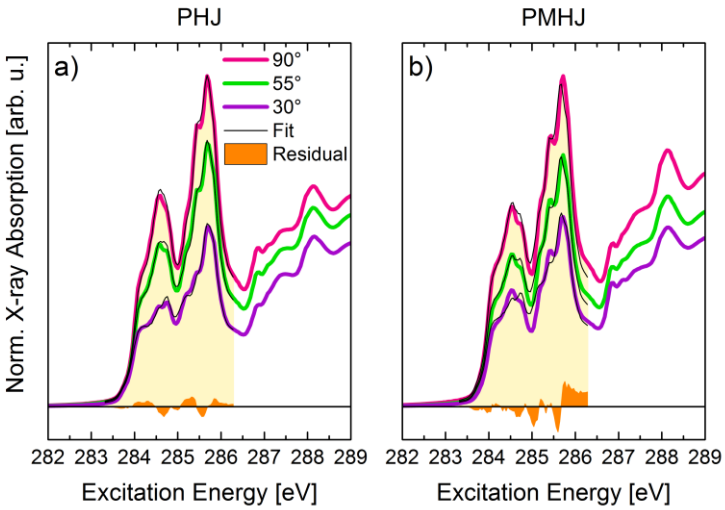

Figure S7 X-ray absorption spectra for device relevant architectures, PHJ (a) and PMHJ (b), of DIP and PDIR-CN_2 on SiO_2. The thin black lines show linear combinations of pristine DIP and PDIR-CN_2 spectra at Θ=55°, providing the best fit to the experimental data. The orange curve is the residual for the deconvolution at Θ=90°. For visual clarity, the absorption spectra for Θ=70° and 40° are not shown.

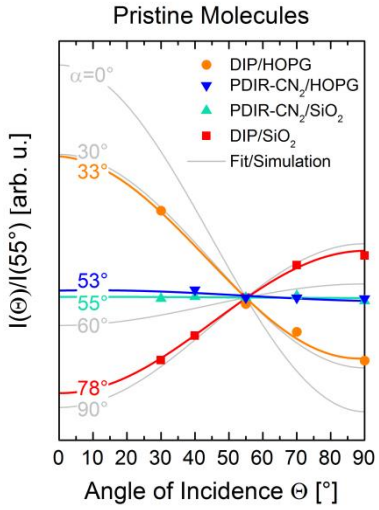

Figure S8 Evaluation of the dichroism (C1s-π* transition) for pristine molecular thin films of DIP and PDIR-CN_2 on substrates SiO_2 and HOPG. The specified angles α on the left are the average inclination angle between molecular and substrate surface plane for each fitted/simulated dichroism curve. The C1s substrate signatures were subtracted prior to the analysis. All curves are normalized to an incident angle of 55° to eliminate the constant of proportionality introduced in eq. 1.

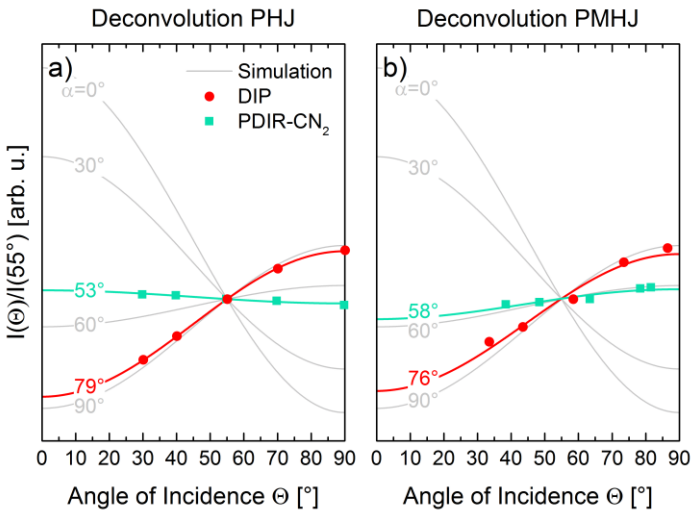

Figure S9 Evaluation of the π*-dichroism shown in figure 5 for the pristine molecular contributions in the device relevant architectures – PHJ (a) and PMHJ (b). The specified angles α on the left are the average inclination angle between molecular and substrate surface plane for each fitted/simulated dichroism curve. The C1s substrate signatures were subtracted prior to the analysis. All curves are normalized to an incident angle of 55° to eliminate the constant of proportionality introduced in eq. 1.

PL transients

Figure S10 shows photoluminescence transients recorded for pristine films of DIP and PDIR-CN_2 and their blends at 2 temperatures. The corresponding 1/e-decay times were extracted by monoexponential fits and are plotted as a function of temperature in the insets. At low temperatures, the average decay time of the pristine films is very long (> 12.5 ns). Therefore, there is a signal contribution at negative delay times. CT-decay of 1:1 blend is faster at RT and slower at 10 K in comparison to PDIR-CN_2-rich blends. No temperature dependence of the PL dynamics in the non-stoichiometric blends is observed.

Ellipsometry

Ellipsometry fit result for mixed films is presented in Figure S11. Both in-plane (Figure S11a, similar to the optical absorption result) and out-of-plane (Figure S11b) components of the extinction coefficient are consistent with the gradual structural transition from standing up-right DIP molecules to tilted PDIR-CN_2 molecules through composition changes. CT bands at 1.4-2.0 eV are visible only for the in-plane component.

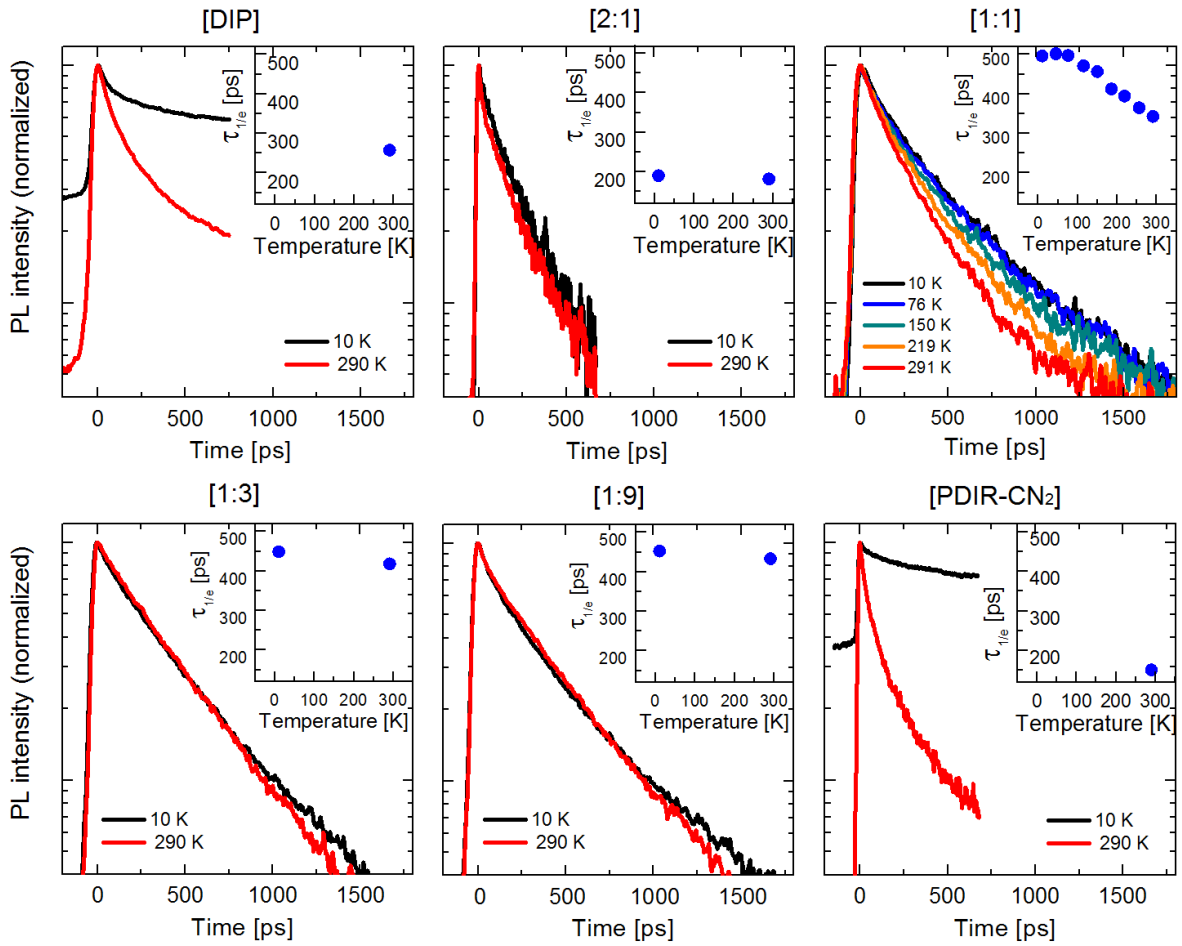

Figure S10 Temperature dependent PL transients. Insets show lifetimes τ versus measurement temperature, τ of pristine DIP and PDIR-CN_2 measured at 10 K Å exceed 12.5 ns and therefore are not shown in the plots.

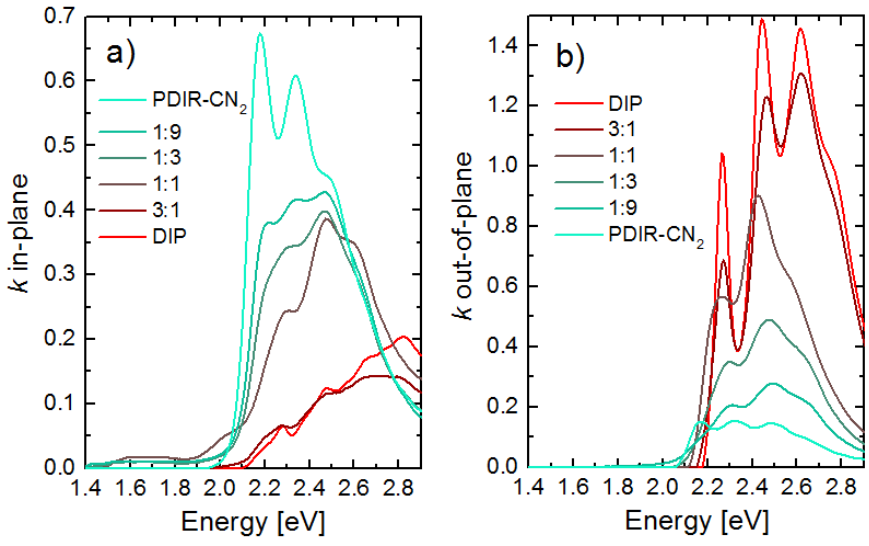

Figure S11 Extinction coefficient *k* evaluated from ellipsometry: (a) in-plane component (parallel to the sample surface) and (b) out-of-plane component (normal to the sample surface).

References

(1) Han, W. N.; Yonezawa, K.; Makino, R.; Kato, K.; Hinderhofer, A.; Murdey, R.; Shiraishi, R.; Yoshida,

H.; Sato, N.; Ueno, N.; Kera, S. *Appl. Phys. Lett.* **2013**, *103*, 253301.
(2) Rangger, G. M.; Hofmann, O. T.; Romaner, L.; Heimel, G.; Bröker, B.; Blum, R.-P.; Johnson, R. L.; Koch, N.; Zojer, E. *Phys. Rev. B* **2009**, *79*, 165306.
(3) Christodoulou, C.; Giannakopoulos, A.; Ligorio, G.; Oehzelt, M.; Timpel, M.; Niederhausen, J.; Pasquali, L.; Giglia, A.; Parvez, K.; Müllen, K.; Beljonne, D.; Koch, N.; Nardi, M. V. *ACS Appl. Mater. Interfaces* **2015**, *7*, 19134–19144.
(4) Opitz, A.; Wilke, A.; Amsalem, P.; Oehzelt, M.; Blum, R.-P.; Rabe, J. P.; Mizokuro, T.; Hörmann, U.; Hansson, R.; Moons, E.; Koch, N. *Sci Rep.* **2016**, *6*, 21291.
(5) Wilke, A.; Amsalem, P.; Frisch, J.; Bröker, B.; Vollmer, A.; Koch, N. *Appl. Phys. Lett.* **2011**, *98*, 123304.
(6) Krause, S.; Schöll, A.; Umbach, E. Org. Electron. 2013, 14, 584–590.
(7) Heimel, G., Salzmann, I., Duhm, S.; Koch, N. Chem. Mater. 2010, 23, 359–377.
(8) Duhm, S.; Heimel, G.; Salzmann, I.; Glowatzki, H.; Johnson, R. L.; Vollmer, A.; Rabe, J. P.; Koch, N. Nat. Mater. 2008, 7, 326 – 332.
(9) Watts, B., Thomsen, L.; Dastoor, P. C. *J. Electron Spectros. Relat. Phenomena* **2006**, *151*, 105–120.
(10) Stöhr, J.; Outka, D. *Phys. Rev. B* **1987**, *36*, 7891–7905.
(11) Opitz, A.; Wilke, A.; Amsalem, P.; Oehzelt, M.; Blum, R.-P.; Rabe, J. P.; Mizokuro, T.; Hörmann, U.; Hansson, R.; Moons, E.; Koch, N. *Sci. Rep.* **2016**, *6*, 21291.
(12) Beyer, P.; Breuer, T.; Ndiaye, S.; Zykov, A.; Viertel, A.; Gensler, M; Rabe, J. P.; Hecht, S.; Witte, G.; Kowarik, S. *ACS Appl. Mater. Interfaces* **2014**, *6*, 21484–21493.
(13) Ferlauto, L.; Liscio, F.; Orgiu, E.; Masciocchi, N.; Guagliardi, A.; Biscarini, F.; Samorì, P.; Milita, S. *Adv. Funct. Mater.* **2014**, *24*, 5503–5510.
(14) Menke, S. M., Lindsay, C. D.; Holmes, R. J. *Appl. Phys. Lett.* **2014**, *104*, 243302.
(15) Clarke, T. M.; Durrant, J. R. *Chem. Rev.* **2010**, *110*, 6736–6767.
(16) Vandewal, K.; Goris, L.; Haeldermans, I.; Nesládek, M.; Haenen, K.; Wagner, P.; Manca, J. V. *Thin Solid Films* **2008**, *516*, 7135–7138.
(17) Benson-Smith, J. J.; Goris, L.; Vandewal, K.; Haenen, K.; Manca, J. V.; Vanderzande, D.; Bradley, D. D. C.; Nelson, J. *Adv. Funct. Mater.* **2007**, *17*, 451–457.
(18) Bruevich, V. V; Makhmutov, T. S.; Elizarov, S. G.; Nechvolodova, E. M.; Paraschuk, D. Y. J. *Exp. Theor. Phys.* **2007**, *105*, 469–478.
(19) Goris, L.; Haenen, K.; Nesládek; M.; Wagner; P.; Vanderzande, D.; De Schepper, L.; D'haen, J.; Lutsen, L.; Manca, J. V. *J. Mater. Sci.* **2005**, *40*, 1413–1418.
(20) Goris, L.; Poruba, A.; Hod'ákova, L.; Vaněček, M.; Haenen, K.; Nesládek, M.; Wagner, P.; Vanderzande, D.; De Schepper, L.; Manca, J. V. *Appl. Phys. Lett.* **2006**, *88*, 052113.
(21) Seah, M. P.; Dench, W. A. *Surf. Interface Anal.* **1979**, *1*, 2–11.